Astron. Astrophys. 343, 352–366 (1999)

ASTRONOMY AND ASTROPHYSICS

Automated supershell recognition in spiral galaxies employing hydrodynamic simulations

S.Y. Mashchenko[1,⋆], **D.A. Thilker**[2], **and R. Braun**[1]

[1] Netherlands Foundation for Research in Astronomy, Postbus 7990 AA, Dwingeloo, The Netherlands (e-mail: syam@phy.ulaval.ca, rbraun@nfra.nl)

[2] Department of Astronomy, New Mexico State University, Box 30001 / Dept 4500, Las Cruces, NM 88003-8001 (e-mail: dthilker@nmsu.edu)

Received 29 May 1998 / Accepted 20 November 1998

Abstract. The search for expanding supershells in nearby galaxies has been the focus of substantial observational effort since the discovery of huge HI bubbles in the Magellanic clouds. Until recently, studies of this nature were limited: initially due to the lack of detailed models describing the predicted appearance of supershells, subsequently because it is challenging to quantify the similarity of model and data over numerous channel maps by visual inspection. Thilker et al. (1998a) first established a method for automated identification and classification of supershells in spiral galaxies. Their object recognition technique is capable of locating complex 3-dimensional patterns in a spectral-line datacube via cross-correlation analysis. We report on various refinements to the basic method and discuss the implications for one particular galaxy (NGC 2403). Most significantly, we now incorporate realistic hydrodynamic models of superbubble structure. We also introduce more robust treatment of shell significance, especially for the case of overlapping structures.

Key words: infrared: galaxies – galaxies: ISM – galaxies: individual: NGC 2403 – ISM: bubbles – methods: data analysis – hydrodynamics

1. Introduction

Since the pioneer work of Heiles (1979), expanding HI supershells have been recognized as common features of interstellar medium (ISM). Superbubbles are observed both in the Milky Way (Heiles 1979) and in other spiral (Brinks & Bajaja 1986; Deul & den Hartog 1990; Kamphuis et al. 1991; Ryder et al. 1995; Lee & Irwin 1997) and irregular (Goudis & Meaburn 1978; Meaburn 1980; Puche et al. 1992) galaxies. These observational efforts were motivated by the importance of supershells for understanding global structure and evolution of the ISM. It has been shown (Mashchenko & Silich 1994) that superbubbles can cause formation of giant molecular clouds and thus represent an underlying mechanism for stochastic self-propagating star formation (SSPSF). Radial gradients in the age of stars detected within some supershells (Oey & Massey 1995; Bomans et al. 1995) serve as observational evidence for SSPSF. Superbubbles also seem to be an important source of hot enriched gas for halos of big galaxies (Wang et al. 1995) and even the intergalactic medium (Heckman et al. 1995). The recent idea that some supershells may result from gamma-ray bursts (Loeb & Perna 1998) draws even more attention to the problem of detection of these structures.

Recent years have witnessed the development of sophisticated hydrodynamic simulations describing the evolution of expanding superbubbles. A few representative modeling efforts are reported in Mac Low & McCray (1988), Tomisaka (1992), and Silich et al. (1996). These simulations can predict the kinematic signature and projected appearance of shells evolving within complex, specified environments. From an observational perspective, numerical supershell modeling allows one to constrain properties of the ISM wherever a bubble is found. Such application of hydrodynamic simulations nevertheless demands comparing a complicated 3D theoretical model with observational data.

This promising aspect of superbubble simulations has remained largely overlooked because it is difficult to assess detailed similarity between numerical models and a spectral-line datacube. Until recently, most studies focused on determination of supershell radius and expansion velocity because these parameters are relatively easy to estimate. Brinks & Bajaja (1986), Deul & den Hartog (1990), and Puche et al. (1992) are among the classic papers which showed it was possible to find "holes" and shells in HI maps of nearby galaxies. Unfortunately, these early studies treated the line-of-sight expansion velocity as a representative, mass-averaged quantity. Such an assumption is reasonable for small shells, but as bubbles grow non-spherical the expansion velocity becomes highly dependent on direction. Significant uncertainties in the determination of shell mass also made it difficult to accurately estimate kinetic energy. Thilker et al. (1998a, hereafter TBW98) developed the first repeatable and statistically robust method of directly comparing supershell models with observational data. TBW98 employed a three-dimensional datacube cross-correlation algorithm in order to locate and characterize superbubble structures in NGC 2403.

Send offprint requests to: S.Y. Mashchenko

⋆ *Present address:* Département de Physique and Observatoire du Mégantic, Université Laval, Québec, Qc., Canada, G1K 7P4

Their analysis suggested that NGC 2403's current supershell population is consistent with the rate of mechanical energy deposition expected from massive stars. Furthermore, they confirmed that stalled shells have a median in-plane size about 2 times larger than shells which still expand. TBW98 also presented evidence for "HI froth" composed of incomplete shell filaments.

This paper is a natural extension of the TBW98 cross-correlation based supershell analysis. Specifically, the simple models used by TBW98 were intended to demonstrate the object recognition technique. We now improve upon the original datacube cross-correlation method by incorporating hydrodynamic shell simulations as the template to which data are compared. In addition, this paper describes a few other subtle but important refinements. Most of these secondary changes are related to the way we measure the significance of any particular structure and how overlapping shells are treated.

The text is organized as follows. In Sect. 2, we describe the shell model properties important for the following analysis. The discussion in Sect. 3 centers on modifications to the object recognition algorithm. Sect. 4 presents details of how we applied the modeling code to generate a collection of supershells tuned for NGC 2403. We give an explicit description of the parameter-space survey, indicating assumptions for the quiescent ISM. In Sect. 5, we briefly discuss the observed population of supershells in NGC 2403 and compare our results to those of TBW98. We conclude with a summary in Sect. 6.

2. Numerical modeling scheme

The thin-shell approximation has been intensively used in interstellar medium physics to simulate expanding shells and supershells which arise in response to the localized injection of mechanical energy (e.g. due to strong stellar winds and/or supernova explosions) into the ISM. (See an excellent review on the subject by Bisnovatyi-Kogan & Silich 1995.) Both two-dimensional (Bisnovatyi-Kogan & Blinnikov 1982, Mac Low & McCray 1988) and three-dimensional (Bisnovatyi-Kogan & Silich 1991, Silich 1992) implementations of the thin-layer algorithm have been developed.

Mac Low et al. (1989) showed that thin-shell predictions regarding general superbubble properties remain rather accurate for some time even after blowout phenomena (strong acceleration of bubble caps in the stratified ISM) and fragmentation caused by Rayleigh-Taylor instabilities. The same authors indicated the thin-shell code is many orders of magnitude faster than a corresponding fluid dynamic numerical scheme, making it the code of choice for bubble simulations in a multidimensional parameter space (Silich et al. 1996). This important property was the basic reason we decided to use the thin-layer algorithm in our automated shell recognition package.

The adopted thin-shell model of superbubble evolution and our galactic model are described in Appendices A and B. The basic parameters determining bubble structure for any moment of time t are: $L_{\rm OB}$ – mechanical luminosity of the parental OB-association; $M_{\rm g}$, r_0 and z_0 – the mass, length scale, and height scale of the galactic disk; T_0 and ρ_0 – in-plane temperature and density of the quiescent gas; $C_{\rm pr}$ – ratio of total versus thermal pressure (assumed constant) for the undisturbed ISM; $T_{\rm halo}$ is the temperature of the hot halo at height $z_{\rm halo}$.

To enable the direct comparison between simulated bubbles and an observed distribution of neutral hydrogen, we needed a way to project the simulated HI distribution (defined in spatial 3D space, XYZ) onto the observational frame of reference (with two projected spatial, $X'Y'$, and one velocity, V, dimensions). For this purpose we designed a smoothed-plates projection algorithm (Appendix C).

It can be shown that in our numerical scheme, the coordinates and velocities of shell elements are not independent functions of the mechanical luminosity, $L_{\rm OB}$, and the density of quiescent gas, ρ_0, but depend only on the ratio $L_{\rm OB}/\rho_0$. In other words, if $\rho_0' = \beta\rho_0$ and $L_{\rm OB}' = \beta L_{\rm OB}$, where β is an arbitrary constant, then

$$\begin{aligned} \mathbf{r}'(L_{\rm OB}', \rho_0') &= \mathbf{r}(L_{\rm OB}, \rho_0), \\ \mathbf{V}'(L_{\rm OB}', \rho_0') &= \mathbf{V}(L_{\rm OB}, \rho_0), \\ N_j'(L_{\rm OB}', \rho_0') &= \beta N_j(L_{\rm OB}, \rho_0). \end{aligned} \quad (1)$$

Here $\mathbf{r}$ and $\mathbf{V}$ represent the coordinates and velocity vector of shell elements. N_j is a column density of projected HI distribution in j-th velocity channel.

This property helps to dramatically reduce the amount of computational time spent for cross-correlation of simulated bubbles with the observational data, because it allows elimination of the "ρ_0" axis in our initial parameter space. One drawback of such an approach is that we cannot introduce into the model those physical processes which are non-linear functions of gas density. The most important of them are radiative cooling of hot gas inside the remnant (following Silich et al. 1996) and self-gravity of undisturbed and shocked gas. Both are proportional to the square of the gas density.

In Fig. 1 we show volume rendered supershell models that have been calculated for two different positions within a galactic disk. In particular, we computed simulations appropriate to galactocentric radii of 2.5 kpc (Sequence A) and 5.0 kpc (Sequence B) in a disk having $M_{\rm g} = 7.6 \times 10^9\ M_\odot$, $r_0 = 2.5$ kpc, $z_0 = 0.25$ kpc, $C_{\rm pr} = 4$, and $z_{\rm halo} = 10$ kpc. All shells were assumed to have a mid-plane origin. For each position, we show a sequence in age of 5, 10, 20, 30, and 40 Myr. We assumed $\rm L_{OB} = 0.32 \times 10^{38}$ erg s^{-1}, corresponding to one supernova every million years.

Several points are noteworthy and demonstrate the accuracy of our modeling code: (1) As expected, our youngest shells appear nearly spherical, although size and expansion velocity change with $L_{\rm OB}$ and the HI scale height. For reference, Table 1 lists mass-averaged, in-plane, and out-of-plane radii and expansion velocities for each shell in Fig. 1. (2) Bubbles in regions of reduced disk thickness become highly non-spherical more quickly than bubbles evolving in fluffy gas distributions. The FWHM thickness of the HI layer is 250 pc for our models at $R_{\rm g}$ = 2.5 kpc and 575 pc for models at $R_{\rm g}$ = 5.0 kpc. (The difference between these FWHM dimensions is substantial because the galactocentric distances associated with Sequence A and B are

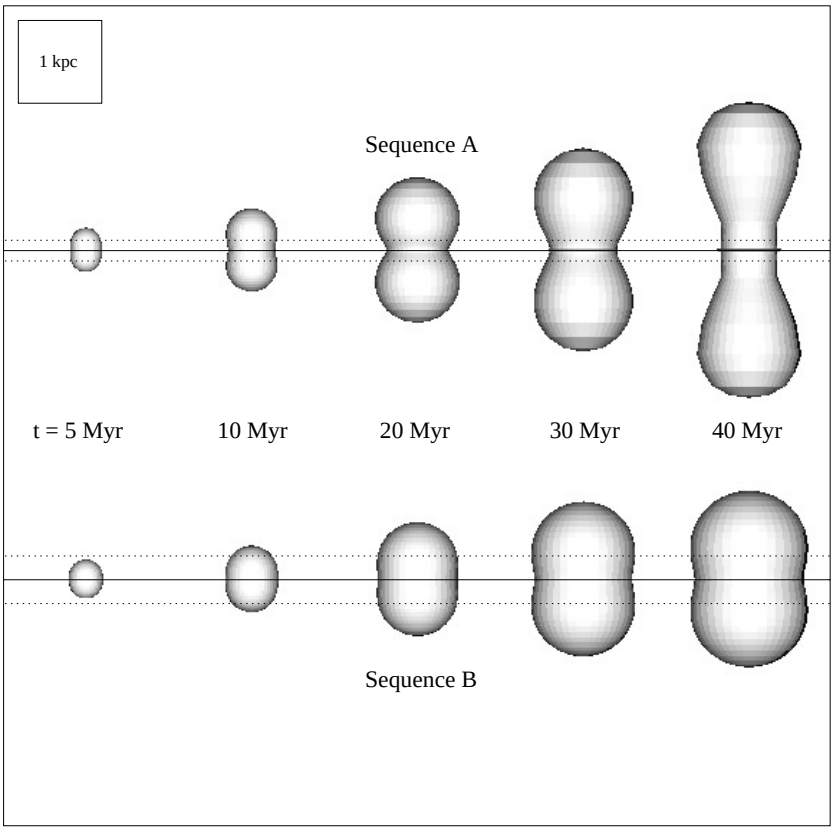

Fig. 1. Volume-rendered supershell models, presented in the form of 2 independent time sequences. The bubble models were computed assuming mechanical luminosity input appropriate to a rate of one supernova every 10^6 years. This energy source was turned off at t = 30 Myr. Sequence A shows the evolution in a disk with HI FWHM thickness $\sim$ 250 pc, as indicated by the dotted lines. Sequence B shows what happens in a disk with FWHM thickness $\sim$ 575 pc. Table 1 indicates the supershell in Sequence A begins blowout by 30 Myr.

Table 1. Shell radii and expansion velocities

Shell type	$R_{\rm avg}$ (pc)	$V_{\rm avg}$ (km s^{-1})	$R_{\rm in}$ (pc)	$V_{\rm in}$ (km s^{-1})	$R_{\rm out}$ (pc)	$V_{\rm out}$ (km s^{-1})
$R_{\rm g} = 2.5$ kpc, $t = 5.0$ Myr	265	32	236	24	332	52
$R_{\rm g} = 2.5$ kpc, $t = 10$ Myr	403	21	327	14	586	46
$R_{\rm g} = 2.5$ kpc, $t = 20$ Myr	576	10	422	5.6	1007	38
$R_{\rm g} = 2.5$ kpc, $t = 30$ Myr	579	-7.3	443	-0.64	1323	45
$R_{\rm g} = 2.5$ kpc, $t = 40$ Myr	448	-16	381	-7.3	1774	58
$R_{\rm g} = 5.0$ kpc, $t = 5.0$ Myr	305	36	292	32	330	44
$R_{\rm g} = 5.0$ kpc, $t = 10$ Myr	462	27	426	22	533	36
$R_{\rm g} = 5.0$ kpc, $t = 20$ Myr	687	18	600	13	860	28
$R_{\rm g} = 5.0$ kpc, $t = 30$ Myr	846	15	714	9.7	1139	27
$R_{\rm g} = 5.0$ kpc, $t = 40$ Myr	952	3.4	793	5.0	1297	-2.8

1 and 2 units of the adopted disk scale-length r_0, respectively.) (3) After the powering OB association turns off at $t = 30$ Myr, our simulations suggest that superbubbles may eventually begin to shrink. Shrinkage is predicted to be most prominent in the galaxy mid-plane, where external ambient pressure is at a maximum. Note that the thin-shell approximation we employ does not allow bubbles to fragment. Fragmentation could substantially mitigate shrinkage. (4) Our time sequence A for $R_{\rm g}$ = 2.5 kpc in Fig. 1 illustrates the "blowout" process. On the other hand, sequence B (Fig. 1) shows a structure insusceptible to blowout. For this particular case Table 1 indicates that the out-of-plane expansion velocity becomes negative by t = 40 Myr due to a combination of substantial ambient pressure at high z, and gravitational deceleration associated with the galactic disk. (5) Finally, we note how difficult it is for the in-plane superbubble cavity to achieve a very large diameter for realistic HI disks and input energies. In most cases, blowout occurs (reducing internal pressure) or the entire shell stalls (due to lack of energy input) before in-plane superbubble size can become exceptional. Maciejewski & Rozyczka (1993) examined the effect of a physically extended power source for supershells but still had difficulty explaining a large structure in M101 described by Kamphuis (1993).

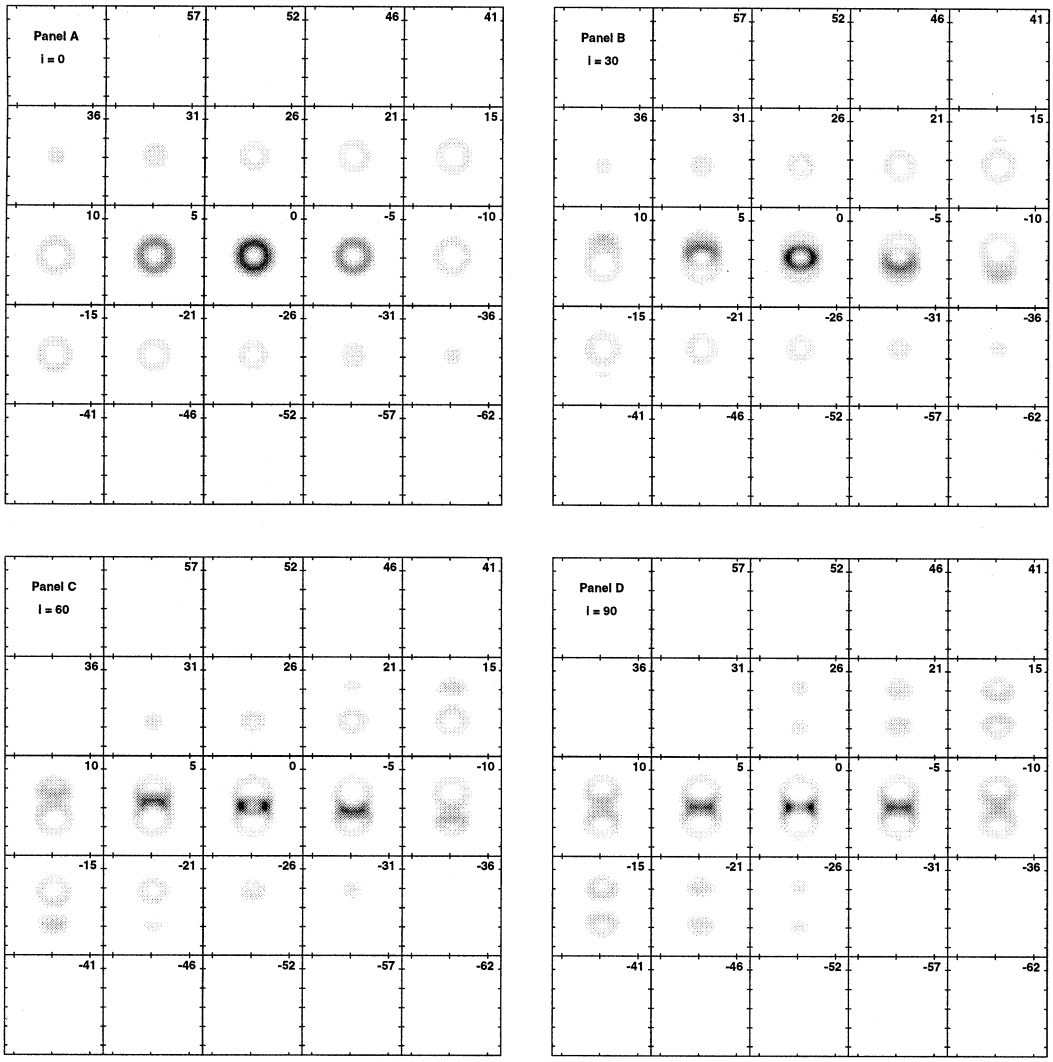

Fig. 2a–d. Simulated channel maps for the center model of Sequence A in Fig. 1. Panels **a–d** show the projected appearance at four different inclinations, 0, 30, 60, and 90° respectively. This model has $R_{\rm avg}$ = 576 pc and $V_{\rm avg}$ = 10 km s^{-1}. The spatial resolution is 150 pc and each channel map is separated by $\sim$ 5 km s^{-1}. The assumed galaxy major axis is horizontal, and the near side minor axis points downward.

Fig. 2 illustrates the projected 21-cm appearance of a model HI bubble as viewed at 4 different inclinations. In particular, the featured supershell is the center structure of Sequence A in Fig. 1. It has $R_{\rm avg}$ = 576 pc, $V_{\rm avg}$ = 10 km s^{-1}, and t = 20 Myr. Smoothed-plate projection of this model was completed for viewing angles of i = 0, 30, 60, and 90°. The resulting cubes are displayed in panels (a)-(d) of Fig. 2, respectively. Each panel shows a sequence of channel maps separated by $\sim$ 5 km s^{-1}. The host-galaxy major axis was assumed to be horizontal, the near-side minor axis extends downward, and we use a beamsize corresponding to 150 pc FWHM. All of the panels are drawn using the same linear scaling for model intensity.

3. Comparison of models with observational data

In the absence of previously confirmed supershell positions, the problem of comparing numerical models with a spectral-line datacube initially reduces to an exercise in 3D pattern (object) recognition. We first locate regions within the observed datacube which are reasonably similar to each of our models. Subsequently, having compiled a list of possible shell detections, one might choose to fine-tune the best-match model for each candidate through a detailed fitting procedure. In the section below, we initially discuss cross-correlation-based 3D object recognition and then examine how to make sense of the results, focusing on measures of detection significance and shell completeness. Two methods for comparing model and data when shell positions are known are suggested in Thilker (1998).

3.1. Cross-correlation

Two-dimensional object recognition techniques have been widely explored for non-astronomical applications. Fields related to the subject include: remote sensing, optical character recognition, and fingerprint matching. An excellent review of relevant techniques is provided by Ritter & Wilson (1996). In

particular, see Sects. 9.1–9.3 of their text. The image-plane and frequency domain correlation methods described therein can be trivially extended to 3 dimensions. Since datacubes produced by interferometric imaging are quite large ($N > 512^2 \times 64$) and the time required for image-plane correlation scales with the square of the number of pixels involved, only pattern matching in the frequency domain is practical in our context. Ritter & Wilson (1996) present several variants of this idea.

TBW98 demonstrated that the simplest possible frequency-based spatial correlation of an image cube and a template pattern can be used to effectively pinpoint those locations where 3-dimensional data are consistent with a template model. The correlation was computed by taking advantage of the convolution theorem, which states that multiplication in the frequency-plane is equivalent to convolution in the image-plane. Taking the complex conjugate of one transform, we note the spatial cross-correlation equals:

$$d \oplus t = FT^{-1}(\hat{d} \cdot \hat{t}^*), \tag{2}$$

where d is the input datacube, t is a template pattern having identical size and dimensionality, $FT(d)$ is given by $\hat{d}$, and $\hat{t}^*$ is the complex conjugate of $FT(t)$. Regrettably, the value of this basic cross-correlation function at any particular pixel in the (processed) output cube not only measures the degree to which data and model agree at that position, but also scales linearly with the original levels of the (unprocessed) datacube. Furthermore, we note that the correlation signal is directly proportional to the auto-correlation of our template cube. These subtleties were known during the analysis described in TBW98. A high-pass exponential taper of $\hat{d}$ was used to remove the dependence on background level. Proportionality with respect to the template auto-correlation was eliminated by normalizing the correlation signal levels with the auto-correlation peak.

Ritter & Wilson (1996) describe a similar technique which they call symmetric, phase-only matched filtering (SPOMF). This method, introduced by Chen et al. (1994), naturally removes the systematic problems noted above and was therefore an attractive alternative to the procedure of TBW98. Ritter & Wilson (1996) also claim it produces sharper correlation peaks. The SPOMF algorithm requires computation of:

$$FT^{-1}\left(\frac{\hat{d}}{\mid \hat{d} \mid} \cdot \frac{\hat{t}^*}{\mid \hat{t}^* \mid}\right), \tag{3}$$

where $\mid \hat{d} \mid$ and $\mid \hat{t}^* \mid$ are the complex amplitude of $\hat{d}$ and $\hat{t}^*$, respectively.

We evaluated the effectiveness of SPOMF in a controlled way by inserting the 3D signature for shells of specified peak brightness into a datacube section covering the center of a spiral galaxy. These slightly modified data were then processed using both SPOMF and TBW98's filtered cross-correlation procedure (FCC). Our tests clearly showed that in the noise-limited regime FCC is intrinsically superior. Consequently, we elected to use TBW98's original cross-correlation procedure for computation of the processed datacubes which delineate the locations of tentative shell detections.

Beyond this point in the processing, we introduced a few refinements in order to: (1) more accurately tabulate tentative shell positions, (2) improve assessment of shell detection significance and completeness, and (3) handle overlapping shells in a manner which guarantees no HI emission is ever "counted" twice by overlapping neighbors. We first describe how every high-pass filtered, cross-correlated datacube is analyzed.

3.2. Source extraction

TBW98 used sequential fitting and subtraction of 2D Gaussian peaks in each plane of an FCC datacube, down to a peak intensity of only a few times the standard deviation. After the fact, these positions were intercompared to determine which families of 2D peaks were actually pointing to the same 3D peak, and thus to the same shell structure.

We have improved upon the method of TBW98 by employing a simplified 3D CLEAN of each processed datacube to identify potential shell positions. (CLEAN is an iterative beam removing technique used to deconvolve radio synthesis observations, originally proposed by Högbom 1974; see also Cornwell & Braun 1989.) We use the high-pass filtered, auto-correlation (FAC) of each model as our CLEAN beam after setting negative regions to zero. The scaled CLEAN beam is iteratively subtracted at the location of the current peak in the FCC data until no pixels exceed a specified significance threshold. This procedure is more robust against detection of false secondary peaks ("sidelobes") in the cross-correlated response, allowing us to detect adjacent shells with similar properties. Negative regions of the beam are set to zero in order to prevent negative sidelobes of the auto-correlation from introducing spurious detections near very bright peaks. The net result is a list of CLEAN components for the processed cube associated with each model. The pixel location assigned to each component is the site of a tentative supershell detection having properties similar to the model under consideration.

3.3. Detection significance and shell completeness

Although the value of a cross-correlation function peak is in some sense proportional to the "matching mass", it can not be directly interpreted as a measure of significance or "goodness of fit". Consider an observed structure with a very large mass which poorly matches one of our models. After our CLEAN procedure such a structure could appear more prominent than a perfectly matching, low mass bubble. To distinguish between these two cases, and in order to accurately quantify shell completeness, one needs to determine how well the predicted intensities match the observed ones. Pearson's linear correlation coefficient r is often used for this type of assessment in engineering applications of object recognition. It has been shown that r is a very robust measure of the "goodness of fit" when the data are contaminated by noise (see e.g. Betke & Makris 1995). By definition, the normalized correlation coefficient is

$$r_j = \frac{cov(t_j, d)}{\sqrt{var(t_j)var(d)}}. \tag{4}$$

In this expression, cov represents the covariation operator, while var denotes variation. As before, d is the observational datacube and t_j is one of our template models. Our numerous tests showed that in the presence of dependent noise in the data (having standard deviation σ) a robust estimator $\tilde{r}_j$ of the normalized correlation coefficient can be obtained by replacing the $cov(t_j, d)$ and $var(d)$ in the Eq. (4) with their expected values (corrected for the presence of noise):

$$\begin{aligned}\tilde{r}_j \;=\; & \left(\sum t_{ij}d_i - \frac{1}{N}\sum t_{ij}\sum d_i\right)\times \\ & \times\;\left[\sum t_{ij}^2 - \frac{1}{N}\left(\sum t_{ij}\right)^2\right]^{-\frac{1}{2}}\times \\ & \times\;\left[\sum d_i^2 - \frac{1}{N}\left(\sum d_i\right)^2 - \sum\sigma_i^2\right]^{-\frac{1}{2}}. \end{aligned} \quad (5)$$

When calculating $\tilde{r}_j$ for each tentative detection, we take only a small part of the observational data-cube which contains the particular bubble. N is defined as the number of pixels in this subcube.

The noise-corrected estimator $\tilde{r}$ obtained using Eq. (5) is an invariant of linear transformations of the function t_j. A linear transformation of t_j can be written as

$$t'_{ij} = \alpha_j + \beta_j t_{ij}, \quad (6)$$

where α_j and β_j are constants. This important property of the coefficient $\tilde{r}$ will be used in Sect. 3.4. Even though we still confront a fundamental signal-to-noise limit for detecting faint structures (during the CLEANing of processed cubes), use of the correlation coefficient removes any bias against shells evolving in low column density regions during the ranking of tentative detections.

There are other advantages of this direct approach. First, we eliminate all uncertainties related to high-pass filtering. Furthermore, $\tilde{r}$ should be directly related to the degree of shell completeness indicated by our observations. As we show at the end of Sect. 3.4, this relation can be explicitly quantified with simulated data. Direct computation of the correlation coefficient also allows us to introduce pixel-by-pixel weighting while using (5). For example, we might wish to give more weight to high-velocity parts of the shell, in order to explicitly confirm out-of-plane filaments.

To summarize, the method of TBW98 is appropriate for finding shell *candidates*, but the direct analysis described above is required in order to fairly choose the best-matching detections. It also gives us a rigorous handle on shell completeness. Below is a description of how we incorporated Eq. (5) into the overall object recognition method.

CLEANing of the FCC datacubes provides a list of candidate shell detections for each model considered. Within each list, we sort the candidates by signal-to-noise and exclude abnormally close neighbors. (Even the cross-correlation peak of a very solid detection will not be exactly represented by the model auto-correlation, leading to a small group of "candidates" surrounding the true position of a well-matched structure.) For every model, beginning with the highest signal-to-noise detection in the list, we eliminate all lower signal-to-noise candidates (of the same type) with a center position falling inside the FWHM volume of the model FAC. We iterate over remaining candidates in the list, giving progressively lower signal-to-noise candidates a chance to eliminate their own close neighbors.

After individual lists have been processed to remove neighbors, we compute the noise-corrected value of the correlation coefficient, $\tilde{r}$, for each candidate using Eq. (5). To speed up the process, we only take along pixels for which the predicted model intensity is greater than 0.1% of the datacube standard deviation. Based on $\tilde{r}$, we rank the candidates in order of decreasing quality. Finally, an exclusion algorithm similar to that described above is used to identify the best-matching model for each structure in the data. In this case we use the model FAC appropriate to the highest-ranking candidate. It is important to note that this procedure is equivalent to completing a detailed fit of several models to each candidate. Any model which is even slightly well-matched to the data at the position of the highest-ranking candidate will have a corresponding candidate in the group defined by the filtered-autocorrelation beam. The best-matched model (as judged by $\tilde{r}$) naturally survives our ranking and exclusion procedure.

3.4. Ensemble optimization

Despite substantial gains associated with the use of $\tilde{r}$ as a measure of detection quality, we still need to be concerned about the effects of overlapping shell filaments. This issue is of great importance because: (1) overlap happens often, (2) estimates of completeness for adjacent bubbles can be artificially high if no correction is made, and (3) global diagnostics such as the total mass or kinetic energy of a shell population would otherwise be overestimated.

Overlapping can result from two main reasons: (1) purely geometrical – crowding of shells along a line of sight (this effect should be stronger for galaxies viewed at high inclination), and (2) physical interaction of the expanding bubbles. In our present work we do not address the second issue (this would require hydrodynamic simulations of interacting bubbles, which is a separate complex problem). Instead we treat the overlap of shells in a self-consistent way, although based solely on a geometrical interpretation of the phenomena.

As we saw in the previous section, the correlation coefficient $\tilde{r}$ has the same value for arbitrary linear transformations of the template function t_j (Eq. (6)). The parameters α_j and β_j corresponding to the best representation of d by t'_j in the least squares sense can be calculated as follows:

$$\beta_j = \frac{\sum t_{ij}d_i - \frac{1}{N}\sum t_{ij}\sum d_i}{\sum t_{ij}^2 - \frac{1}{N}\left(\sum t_{ij}\right)^2}, \quad (7)$$

$$\alpha_j = \frac{1}{N}\sum d_i - \frac{\beta_j}{N}\sum t_{ij}. \quad (8)$$

The additive parameter α_j can be interpreted as a level of local constant background in the data function d. The parameter β_j can be directly related to the bubble model density scaling in-

variant β (Eq. (1)). The best-fit mass of the observed shell $M_{d,j}$ can be estimated as

$$M_{d,j} = \beta_j M_t, \tag{9}$$

where M_t is a mass of the model.

For the vast majority of the observed shells the condition $N\alpha_j \ll \sum \beta_j t_{ij}$ holds. It allows us to neglect the background term in Eq. (8) while designing the iterative shell ensemble optimization procedure. The aim of the procedure is to interpret the observed intensity in the areas of overlap as a sum of intensities from the overlapped shells. To achieve it we split the intensity d_i and standard deviation of the noise σ_i in the following manner:

$$d_{ij} = d_i w_{ij}, \quad \sigma_{ij} = \sigma_i w_{ij}, \tag{10}$$

with a normalizing condition for the weighting function w_{ij}:

$$\sum_j w_{ij} = 1. \tag{11}$$

At every step of our iterative procedure we calculate our estimate for the function w_{ij} on the basis of β_j values obtained at the previous step:

$$w_{ij} = \frac{\beta_j t_{ij}}{\sum\limits_k \beta_k t_{ik}}. \tag{12}$$

New (optimized) values of $\tilde{r}_j$ and β_j can be obtained by replacing the observed intensities d_i and standard deviations of the noise σ_i in Eqs. (5) and (7) with corresponding d_{ij} and σ_{ij} values (Eq. (10)):

$$\tilde{r}_j = \left(\sum t_{ij} d_i w_{ij} - \frac{1}{N} \sum t_{ij} \sum d_i w_{ij} \right) \times$$
$$\times \left[\sum t_{ij}^2 - \frac{1}{N} \left(\sum t_{ij} \right)^2 \right]^{-\frac{1}{2}} \times$$
$$\times \left[\sum (w_{ij} d_i)^2 - \frac{1}{N} \left(\sum w_{ij} d_i \right)^2 - \sum (w_{ij} \sigma_i)^2 \right]^{-\frac{1}{2}}, \tag{13}$$

$$\beta_j = \frac{\sum t_{ij} d_i w_{ij} - \frac{1}{N} \sum t_{ij} \sum d_i w_{ij}}{\sum t_{ij}^2 - \frac{1}{N} \left(\sum t_{ij} \right)^2}. \tag{14}$$

Recomputing $\tilde{r}$ for each candidate shell in such a manner implies that certain detections will likely benefit from the reduction of observed intensity in regions of overlap, while others may be judged less significant.

At some point, we need to adopt a cutoff in $\tilde{r}$ to prevent largely incomplete shells from being catalogued. In light of the discussion above, it is easy to see that statistics and scaling parameters for all candidate detections in a galaxy must be derived in an iterative manner (since the lowest quality shells will occasionally, but unpredictably, fall below our specified cutoff in $\tilde{r}$).

We adopt the following procedure for simultaneous optimization of all shells in a galaxy: (1) compute $\tilde{r}$ for each candidate, using Eqs. (10)–(13), with initial estimate for scaling parameters β_j derived from Eq. (7); (2) discard all candidates for which $\tilde{r}$ is below $\tilde{r}_{\rm crit}$; (3) compute the revised β_j for each surviving detection using Eq. (14); (4) loop back to step (1), but use the new scaling parameters β_j. Iteration continues until no candidate detections are discarded.

It is easy to understand why $\tilde{r}$ should decline for progressively incomplete shells, since the goodness-of-fit will obviously decrease in such cases. To show this trend in a quantitative manner, we undertook numerical simulations with the aim of computing $\tilde{r}$ for shells of varied physical completeness, buried in a realistic noise background. By allowing many trials for each case, we also determined the standard deviation of $\tilde{r}$ as a function of signal-to-noise and completeness.

Our simulations considered a small representative sample of the models from our complete parameter space survey (see Sect. 4.2). We included shells of radically different size and expansion velocity for two contrasting disk environments. Individual models were scaled such that the maximum intensity within a projected shell was 4–10 times the standard deviation of the artificial (beam-smoothed) noise into which they were placed. To simulate incomplete shells, we chose to randomly zero a specified fraction of the model pixels which were originally assigned non-negligible intensities. This step was carried out before the addition of noise. For each type of shell and choice of scaling, we examined fractional completeness values ($f_{\rm com}$) between 0.3 and 1.0. A total of 25 trials were analyzed for each combination of scaling and completeness.

Figs. 3 and 4 illustrate some results from our simulations. For these plots, $\tilde{r}$ was computed using Eq. (5) since all shells were isolated in our tests. We confirmed the following facts: (1) A functional dependence between $f_{\rm com}$ and $\tilde{r}$ can be estimated as $\tilde{r} \sim \sqrt{f_{\rm com}}$ (such a conclusion can be drawn from analysis of Eq. (5) assuming the simplest situation $d_i = {\rm const}$ and $t_{ij} = {\rm const}$), which is in agreement with our test results. Fig. 3 shows a plot of median($\tilde{r}$) versus $f_{\rm com}$. One mark is drawn for each combination of shell type and $f_{\rm com}$ (including only trials with peak S/N = 10). One-sigma error bars are also shown. (2) For realistic choices of model scaling, the standard deviation of $\tilde{r}$ is at most $\sim 10\%$, but declines to less than 2% for a peak signal-to-noise of 10. Fig. 4 illustrates $\sigma(\tilde{r})/\tilde{r}$ as a function of the median signal-to-noise in all parts of a projected bubble. Note that median values of signal-to-noise are generally 5–100$\times$ smaller than the peak signal-to-noise. For this graph, only shells with $f_{\rm com} = 1$ were considered.

The behavior of $\tilde{r}$ and $\sigma(\tilde{r})$ indicated by simulations led us to select $\tilde{r}_{\rm crit} = 0.6$. This value was adopted in order to exclude the majority of structures less than 50% complete.

We also performed tests in which an entire simulated cube was analyzed as if it were real data. This procedure allowed us to put a firm upper limit on the number of shells of each type one might expect to arise by pure chance, given our various cutoffs (S/N and $\tilde{r}_{\rm crit}$). Simulated datacubes were constructed by randomly relocating individual spectra within the actual data, then convolving with the instrumental beam, and adding an appropriate level of Gaussian noise. Spectra from the actual data were relocated with a uniform probability of landing anywhere inside a circle having a radius of 15 pixels centered on the orig-

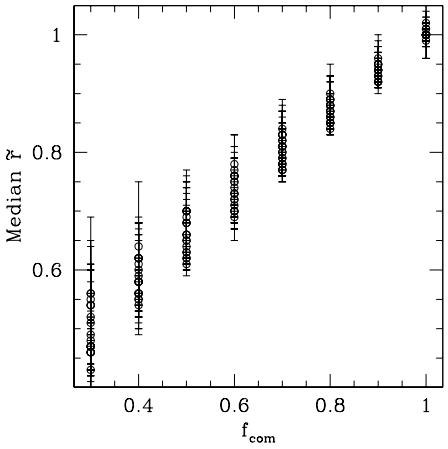

Fig. 3. Median ($\tilde{r}$) versus $f_{\rm com}$. One mark is drawn for each combination of shell type and $f_{\rm com}$ examined during our simulations (including only trials with peak S/N = 10). Each median value of $\tilde{r}$ was computed from a set of 25 trials. In addition, we show one-sigma error bars.

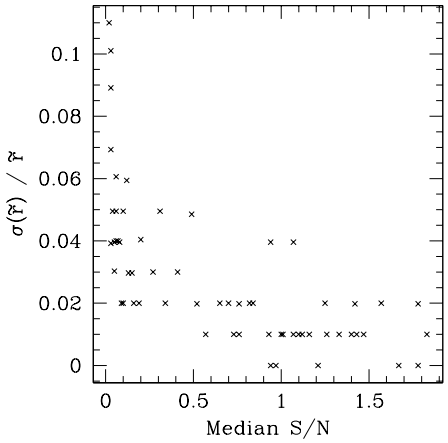

Fig. 4. Our simulations demonstrate that the standard deviation of $\tilde{r}$ decreases with increasing signal-to-noise. One point is plotted for each model included in our test procedure, although we only show trials for which $f_{\rm com}$ = 1.

inal position. In addition, measures were taken to assure that no relocated spectrum was overwritten. The end result of this method is a simulated datacube having all the nominal characteristics of the actual data (noise level, intensity distribution, bulk galactic rotation), but lacking any real structure on scales smaller than $\sim$ 1 kpc.

Processing of these simulated datacubes indicates a total level of contamination (by false detections) of about 5% for our nominal assumptions (S/N = 6, $\tilde{r}_{\rm crit}$ = 0.6). The parameter space distribution of false detections with respect to model type is heavily skewed toward small sizes and low expansion velocities. For instance, contamination specific to shells having $R_{\rm avg}$= 150 pc and $V_{\rm avg}$ = 5 km s^{-1} is $\sim$ 11%, whereas only one false detection was found to have $R_{\rm avg} > 300$ pc. Indeed, for large shells, the level of contamination is less than 1%. Consequently, the vast majority of detections associated with our actual data are thought to be genuine.

4. Parameter space survey

As a test case for our procedure, we analyzed 21-cm observations of the nearby spiral NGC 2403. TBW98 also considered NGC 2403 using an earlier version of the automated supershell recognition software described by this paper. The HI dataset is fully described in Braun (1995).

4.1. Initial considerations

When selecting how to incorporate the hydrodynamic shell models of Sect. 2, our primary concern was to fully explore the range of possible ambient conditions in NGC 2403 and yet retain the smallest possible parameter space to promote quick data processing. This goal requires some simplifying assumptions.

For instance, $C_{\rm pr}$, the assumed ratio of total pressure to thermal pressure within the diffuse medium is not yet well constrained by observational data. The most straightforward parameter space survey would allow $C_{\rm pr}$ to vary. However, in order to bracket a "best guess" value, this implies (at minimum) three times the nominal processing required to derive an HI shell catalog. Other parameters of this nature must also be specified or the computational cost quickly becomes intractable. We elected to fix such "variables" whenever a rough estimate based on theoretical considerations or observational data could be obtained.

4.2. Model assumptions

At any location in the disk of a spiral galaxy, out-of-plane gas density and pressure profiles largely determine the evolution of a superbubble. Steep gradients encourage fast out-of-plane expansion, highly oblate middle-aged shells, and relatively quick "blowout". Flat profiles on the other hand, allow bubbles to retain spherical symmetry for a longer time. Density variation as a function of height above the midplane is a primary influence on the relative brightness of projected shell filaments. In our numerical simulations, vertical density and pressure profiles are a function of two main parameters: $C_{\rm pr}$ and $z_{\rm halo}$, the z distance at which the ambient ISM is assumed to reach a temperature of $T_{\rm halo} = 10^6$ K. The local surface density of the galactic disk is also coupled to the profiles, but is generally well-constrained.

Equipartition of energy would suggest a lower limit of 4 for $C_{\rm pr}$, dividing energy equally between thermal motions, magnetic fields, turbulent motions, and cosmic rays. Recent calculations by Norman & Ferrara (1997) indicate a larger lower limit of about 8. Nevertheless, we took a conservative approach for our simulations, adopting $C_{\rm pr}$=4 with the knowledge that the parameter is likely higher. This uncertainty is not a limiting factor, as density and pressure profiles vary substantially even within a single galaxy. Plausible values for $z_{\rm halo}$ lie in the range from $\sim$ 2–20 kpc. Common sense suggests that this distance might vary among galaxies. We suspect it may depend on galaxy type or star formation rate (SFR) per unit disk area. For lack of a better constraint, we adopted $z_{\rm halo}$=10 kpc in our simulations and used a value of $T_0 = 10^4$ K for the in-plane gas temperature. These parameters are listed in Table 2.

Table 2. Galaxy parameters

Parameter	Value	
Distance	3.2	Mpc
B luminosity	4.25×10^9	$L_\odot$
Stellar disk mass, M_g	7.6×10^9	$M_\odot$
Disk scale length, r_0	2.5×10^3	pc
Disk scale height, z_0	2.5×10^2	pc
Disk/halo interface, z_{halo}	1×10^4	pc
Mid − plane gas temperature, T_0	10^4	K
P/P_{th}, C_{pr}	4	

Table 3. Parameter space survey

Parameter	Value
Galactocentric radius /disk scale length, S	0.1, 1, 2, ...7
Mass − averaged shell radius, R_{avg}	75, 150, 225, ...1125 pc
Mass − averaged shell velocity, V_{avg}	5, 10, 15, ...50 km s^{-1}

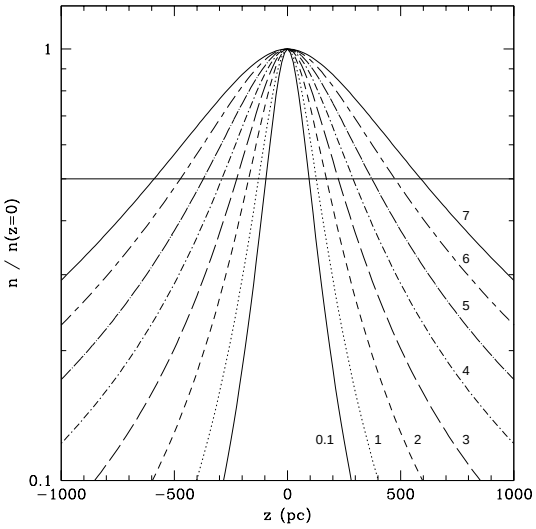

Fig. 5. Out-of-plane density profiles assumed for our NGC 2403 models. Each profile is labeled with a value of S. The FWHM disk thickness ranges from $\sim$ 200–1200 pc.

As noted above, the disk mass per unit area also influences the vertical profile of ambient gas density in our model environment. Given the distance to a galaxy and its total B luminosity, we can estimate the total stellar mass in a system and then derive an estimated surface density at various disk locations. For our calculations we employed the mass-to-light ratio of Bottema (1997), $\Gamma_B = 1.79$. With such a normalization, it is possible to estimate the local surface density of the stellar disk at any galactocentric position to within the error attributable to extinction and any systematic departures from the assumed exponential model of Eq. (B1).

Two remaining galaxy-wide model parameters are radial and vertical scale lengths for the galactic disk. Radial scale length, r_0, can be obtained in the usual way through bulge/disk decomposition. Vertical scale height is a bit more difficult, especially in the presence of substantial extinction (de Grijs et al. 1997). We assumed that r_0/z_0=10, which is close to the values observed in spiral galaxies (de Grijs & van der Kruit 1996). The values adopted for r_0 and z_0 can be found in Table (2).

Fixing C_{pr}, z_{halo}, and the other parameters of Table 2, we were able to significantly reduce the dimensionality of our parameter space survey. Only three parameters were allowed to vary. The first of these we call S, defined to be the ratio of a shell's galactocentric distance and the galaxy's assumed radial scale length. In addition, we varied the obvious parameters of shell radius and expansion velocity. Our particular prescription uses mass-averaged versions of these characteristic variables. In this respect we depart from TBW98, which employed in-plane values.

Table 3 indicates the sampling scheme we adopted to cover this 3-dimensional parameter space. Integral values of S, except for the very inner disk, were selected. The S value of 0.1 was used for computational reasons related to the assumed exponential disk. Grid steps in shell radius were chosen approximately equal to $1/2$ the spatial FWHM of our instrumental beam. Likewise, we selected a linear sampling interval for expansion velocity, allowing for fast-expanding shells with peak radial velocities greater than 50 km s^{-1}. Drawing from this set of models, only fully resolved structures are considered. This restriction is quantified by demanding that the integrated intensity of each allowed model is greater than or equal to 10 times the flux per beam at the position of the brightest peak. Simulations similar to those described in Sect. 3.4 show that our sampling scheme is adequate for initial detection of supershell structures. Generally the value of $\tilde{r}$ drops by less than 25% for a model mismatch of 1 parameter space grid step. During the fine-tuning procedure of Sect. 3.3, one might wish to allow smaller steps in R_{avg} and V_{avg}.

4.3. Implications

Our assumed choices for C_{pr} and z_{halo}, coupled with M_g and the dimensions of the stellar disk, result in vertical gas density profiles having a wide range of FWHM values. For NGC 2403, using S=0.1–7 provides simulated environments with FWHM $\sim$ 200–1200 pc. Values outside of this range are quite unlikely. Fig. 5 shows a density profile for each value of S used in our NGC 2403 survey.

The parameters given in Tables 2 and 3 also specify the out-of-plane pressure variation. For small S values, we obtain rapidly decreasing pressure profiles such as would be expected in regions of high surface density. This type of environment should correspond to the galaxy center or possibly within a spiral arm. Likewise, large values of S produce nearly isobaric pressure profiles. Fig. 6 illustrates these consequences.

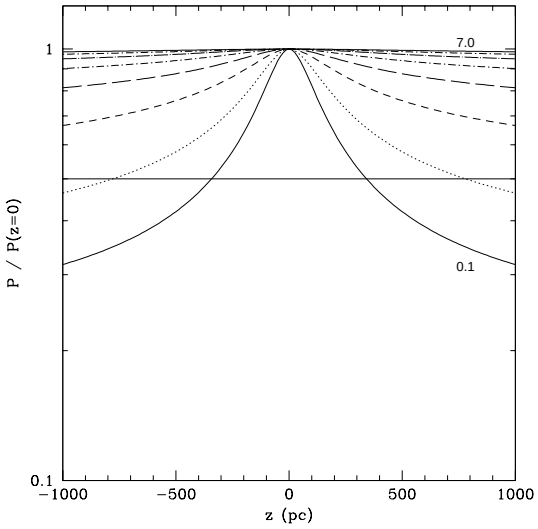

Fig. 6. As in Fig. 5, but for pressure rather than density. Profiles are nearly isobaric for many of the ambient disk models.

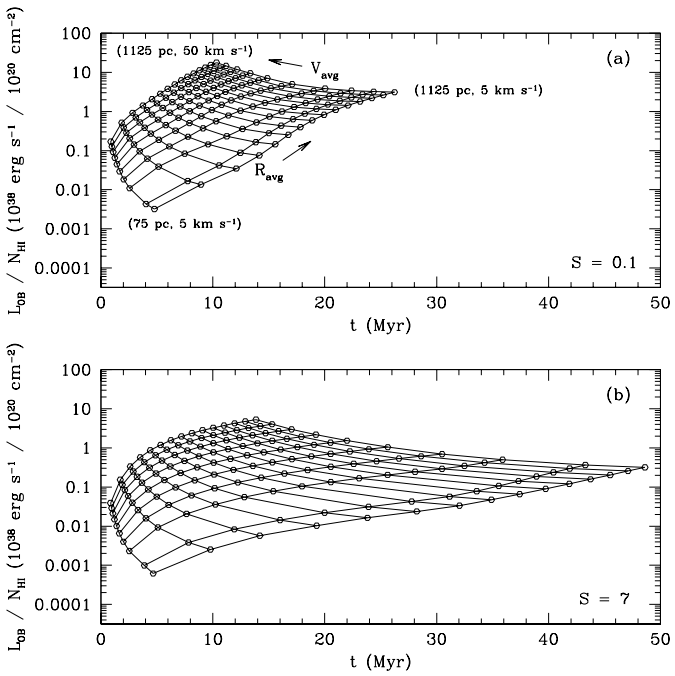

Fig. 7a and b. Panel **a** indicates the relation between (L_{OB}/N_{HI}, t) and (R_{avg},V_{avg}) for each of our NGC 2403 supershell models having S = 0.1. Panel **b** is an analogous diagram for the S = 7 case.

Most supershell modeling has been examined in the context of time-averaged input mechanical luminosity, especially compared to the mean density of ambient gas. We include Fig. 7 in an effort to make the connection between our parameter space and the simulations of previous authors.

Each panel of Fig. 7 shows the inferred values of the ratio L_{OB}/N_{HI}, the mechanical luminosity (in units of 10^{38} erg s^{-1}) divided by the face-on column density (in units of 10^{20} cm^{-2}), as a function of shell age for all 150 (R_{avg},V_{avg}) combinations used in our survey. Specifically, panel (a) of the figure plots the (R_{avg},V_{avg}) grid for S=0.1. The opposite extreme (S=7) is represented in panel (b). We note that in both cases, no shells are older than 50 Myr, although many are old enough for a central OB association to have physically dispersed due to random motions.

5. Supershells in NGC 2403

We do not present a complete scientific discussion of our new results, but only describe changes related to the use of more sophisticated supershell models and other procedural differences. Scientific results for a sample of many galaxies will be presented in a separate paper (Thilker et al. 1998b).

Our procedure differs from TBW98 in that we generate a parameterized decomposition of the observational data, rather than a precise "catalog" of only the highest quality superbubbles. This decomposition is based on a limited set of realistic shell models computed under the assumption of rather idealized conditions. For example, we do not allow dynamical interaction between bubbles and we cannot include the effects of shear due to galactic rotation. Shear significantly influences only the oldest supershells, implying that our algorithm is most sensitive to younger objects. Our parameterized decomposition should be viewed as a well-founded interpretation of the observational data, but certainly not the only possible interpretation consistent with the spectral-line dataset. TBW98 segregated detections into two broad classes: "high-quality" (meaning apparently complete), and "fragmentary". This distinction was made on the basis of signal-to-noise and a rudimentary completeness parameter, β. Our analogous parameter, $\tilde{r}$ serves the same purpose but is significantly more robust, having been extensively tested using simulated data.

Adopting $\tilde{r}_{\rm crit}$ = 0.6 and a minimum signal-to-noise ratio of 6, we detect a total of 601 resolved HI superbubble structures in NGC 2403. Each of these shells is thought to be more than 50% complete (following the discussion of Sect. 3.4). The decomposition is an excellent match to our observational datacube, reproducing a significant fraction of the fine-structure in individual channel maps. Fig. 8 illustrates the spatial distribution of detected superbubbles. We have plotted the observed N(HI) map in panel (a) and show a velocity-integrated version of our composite model in panel (b). Note how the supershells tend to trace spiral structure, suggesting a close link to sites of massive star formation. This is not a selection effect. Before the final iteration to discard incomplete shells, our list of candidate detections included numerous structures throughout the disk, even some located within inter-arm gaps. Recall that $\tilde{r}$ is completely insensitive to changes in linear scaling – it seems the most complete shells are simply located close to the spiral arms. The absence of supershell detections at the tails of spiral arms (Fig. 8, panel B) results from the cutoff on minimum signal-to-noise ratio.

Our parameterized decomposition represents 1.0×10^9 M$_\odot$ of HI, almost $1/3$ the total amount in NGC 2403. In addition, more than 8×10^{53} erg of kinetic energy is associated with supershell expansion. TBW98 identified 50 high-quality shells

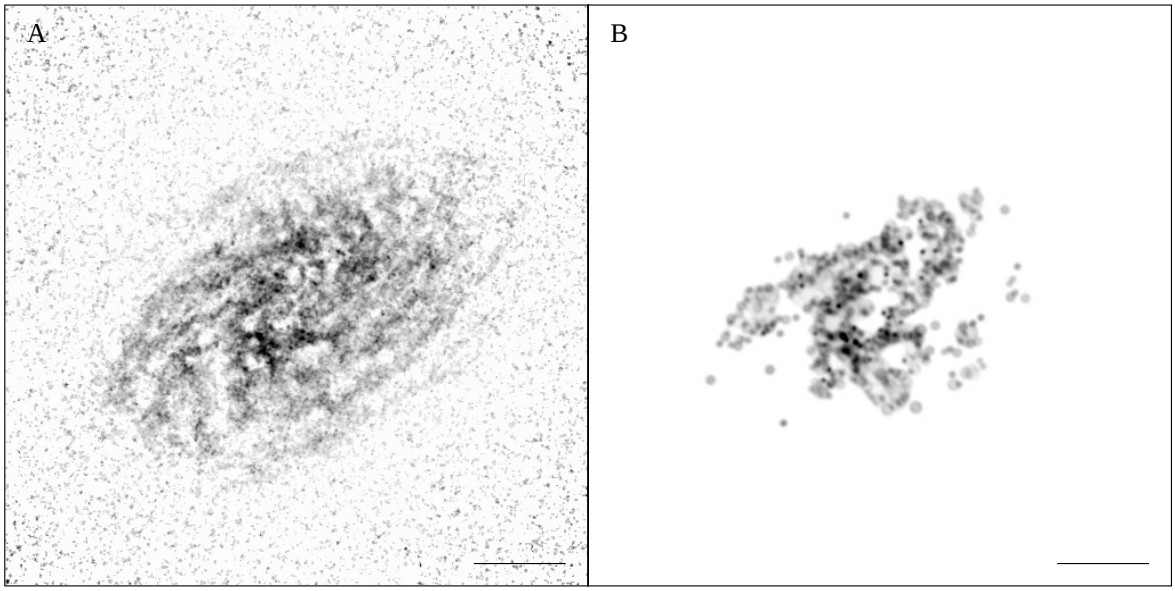

Fig. 8a and b. Panel **a** shows an integrated HI image of NGC 2403. The plot is linearly scaled, with black representing a column density of $\sim 4 \times 10^{21}$ cm^{-2}. Panel **b** presents a velocity-integrated version of our parameterized decomposition (composite model for the entire galaxy). Line segments in the corner of each panel have been scaled to a length of 5 kpc at the distance of NGC 2403. The total field of view is 31.8 $\times$ 31.8 kpc^2 for both panels.

containing 2.1×10^8 M$_\odot$ of HI. In total, TBW98's high-quality and fragmentary shells accounted for 6.7×10^8 M$_\odot$ of HI and more than 2.2×10^{54} erg of kinetic energy. Despite the detection of many more HI shells than TBW98, our estimate of total kinetic energy is substantially smaller. This apparent inconsistency can be resolved by the fact that the majority of the HI shells tabulated in TBW98 were in the "stalled" category, corresponding to the epoch when pressure venting might be expected to have occurred. TBW98 used the modified version of the bubble model of Weaver et al. (1977) which has a constant total-to-kinetic energy conversion factor $k \simeq 0.2$. More accurate simulations show that even for spherical bubbles k can be smaller than 0.1 (Mac Low & McCray 1988), whereas for superbubbles undergoing blowout k can be as low as 0.01 (Igumentshchev et al. 1990).

It is equally instructive to examine differences in the observed distribution of supershell characteristics. Fig. 9 provides histograms of several observed parameters for all the shells in our decomposition. Panel (a) shows that the typical HI mass of an expanding supershell is $\sim$ 1–3 $\times 10^6$ M$_\odot$. This range is slightly less than estimated by TBW98, but our study is more sensitive to small structures and shells evolving in low density environments. The histogram in Panel (b) indicates the structures we detect have exceptionally modest kinetic energies. Recall that the estimated thermal energy content of these bubbles is non-negligible, often dramatically exceeding the energy converted into bulk motion. Note that we do not detect any structures having extraordinary kinetic energy, greater than 10^{53} erg. In contrast to TBW98, we find evidence for a peak in shell kinetic energy just below 10^{51} erg. It seems likely that the enhanced sensitivity of our survey allows this observation, just as in the case of bubble mass. Panel (c) is a histogram of dynamical shell

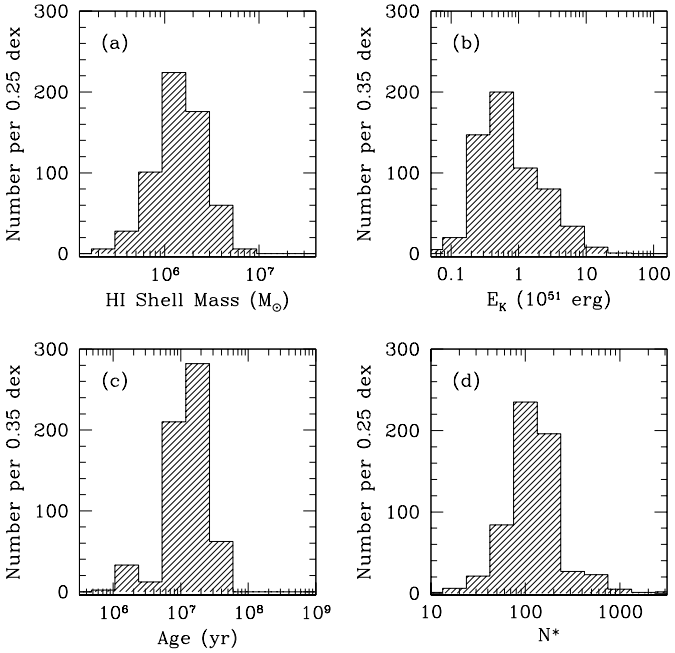

Fig. 9a–d. Histograms showing the characteristics of all HI supershells detected in NGC 2403. Panel **a** indicates an HI mass for each structure. Panel **b** demonstrates that our detections usually have modest kinetic energy. Panel **c** shows the distribution of dynamical age for each structure. Finally, Panel **d** presents the distribution of N$_*$, the number of stars having M $>$ 7 M$_\odot$ needed to power each expanding bubble.

age associated with the best-fit model for each observed structure. We find a sharp peak in the age distribution near 10 Myr, followed by a dramatic decline toward older structures (30 Myr and up). This is probably related to the fact that our models do

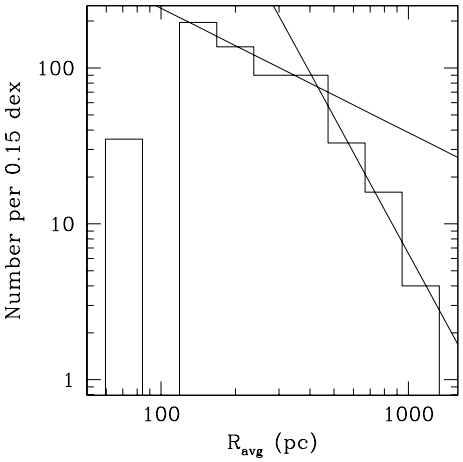

Fig. 10. Distribution of $R_{\rm avg}$ for all HI bubbles in our decomposition of NGC 2403. The data are well-fit by a broken power-law as described by Eq (15). Only shells having $R_{\rm avg} > 100$ pc were included in the fitting procedure.

not allow for shear and the rather small fraction of models having large dynamical age. Nevertheless, there is also some reason to suspect that old bubbles would disintegrate after slowing to near the sound speed. Perhaps the observed age distribution is governed by all of these factors. Finally in Panel (d), we present the distribution of N_*, the required number of progenitor stars with $M > 7\ \mathrm{M}_\odot$, for all shells in our decomposition. The value of this parameter follows directly from the assumed $\mathrm{L}_{\rm OB}$ for each detection's best-fit model and the scaling parameters derived in Sect. 3.4. Although some detected shells require up to $\sim 10^3$ SNe in their progenitor association, the vast majority are well described by simulated bubbles powered via modest groups of 40–200 OB stars. Some of the superbubbles detected by TBW98 required substantially more than 10^3 OB stars. This appears to have been solely a consequence of the simplistic models used in that paper, illustrating the importance of fitting the observational data with realistic projected supershell simulations.

Our decomposition of NGC 2403 is well-suited to analysis of the observed supershell size distribution. Fig. 10 presents a histogram of $R_{\rm avg}$ plotted with log-log scaling. The observed distribution is not well fit with a single power law. We achieve a much better result with a broken power-law having a turnover at $R_{\rm avg} \sim 400$ pc. We have overplotted the following function in Fig. 10:

$$\log\ N(R_{\rm avg}) = \\ = \begin{cases} 4.0\ -\ 0.8\ \log\ (R_{\rm avg}), & \log\ (R_{\rm avg}) \le 2.6, \\ 9.6\ -\ 2.9\ \log\ (R_{\rm avg}), & \log\ (R_{\rm avg}) > 2.6. \end{cases} \quad (15)$$

The uncertainty in both power-law slopes is ~ 0.2. The break in our observed distribution could be related to the disk blowout process. More substantial analysis of the observed superbubble size distribution in a large sample of galaxies, including comparison with the predictions of Oey & Clarke (1997), will be presented in Thilker et al. (1998b).

6. Conclusions

We have refined the method of automated supershell recognition and characterization first introduced by TBW98. The most significant differences between our procedure and that of TBW98 can be summarized as follows: (1) we incorporate realistic numerical simulations for supershell evolution; (2) our analysis of cross-correlated datacubes is now fully three-dimensional, making use of a robust CLEANing algorithm; and (3) we account for projected overlap during the computation of an unbiased estimator for quantifying shell completeness and overall "goodness of fit". The modified procedure has been re-applied to the nearby spiral NGC 2403, where we detect 601 expanding supershells. Each of these structures is more than 50% complete. The conclusions of TBW98 (regarding NGC 2403) appear essentially correct, with only few revisions attributable to procedural differences. Most significantly, we find no evidence for HI supershells requiring OB associations populated by $\sim 10^4$ SNe progenitors.

Acknowledgements. D.A.T. is currently funded as part of the NASA Graduate Student Researchers Program (NGT-51640). This project has also been supported by the following grants: NASA ADP NAG5-2426, NSF AST-91-23777, AST-96-17014. S.Y.M. is grateful to Dr. R. Braun for the invitation, to the whole staff of NFRA for help and friendly assistance during his stay in Dwingeloo.

Appendix A: bubble evolution equations

For our numerical simulations of the bubble evolution, we used a slightly modified version of the 3D algorithm proposed by Silich (1992) which is based on the thin layer approximation. In this method an initially spherical shell is divided in N (typically ~ 1600) Lagrangian surface elements. For each element we use the following differential equations to express the time rate of change of mass, velocity, and position:

$$\frac{\mathrm{d}m}{\mathrm{d}t} = H\left(\frac{\mathbf{Un}}{c} - 1\right)\ \rho\,\mathbf{Un}\,\Sigma, \quad (A1)$$

$$\frac{\mathrm{d}\mathbf{U}}{\mathrm{d}t} = \frac{1}{m}\left[\mathrm{P}_{\rm in} - H\left(\frac{\mathbf{Un}}{c} + 1\right)\ \mathrm{P}\right]\ \mathbf{n}\,\Sigma - \\ -\frac{1}{m}\frac{\mathrm{d}m}{\mathrm{d}t}\,\mathbf{U} + \mathbf{g}, \quad (A2)$$

$$\frac{\mathrm{d}\mathbf{r}}{\mathrm{d}t} = \mathbf{U}. \quad (A3)$$

Here $\mathbf{r}, \mathbf{U}$, and m are defined as the radius-vector, vector of velocity and mass of the Lagrangian element. The unit vector normal to the shock front is denoted as $\mathbf{n}$. Σ represents the element surface area. Density, total pressure and sound speed for the undisturbed medium are given by ρ, P and c, respectively. For mon-atomic gas $c = \sqrt{5kT/3\mu}$, where T is the temperature of the gas. $\mathbf{g}$ denotes the acceleration vector of the external gravitational field. H is the Heaviside step function. The undisturbed gas is assumed to be at rest. We calculate $\mathrm{P}_{\rm in}$, the pressure of the hot gas inside the remnant, from the thermal energy of the gas, $E_{\rm th}$, and the volume of the cavity, Ω: $\mathrm{P}_{\rm in} = 2E_{\rm th}/3\Omega$.

Assuming 10% of helium atoms by number, the averaged mass per particle, μ, was estimated as $\mu = 14/11 m_{\rm p}$, where $m_{\rm p}$ is the mass of a proton.

Eq. (A1) describes sweeping of the undisturbed gas by supersonically moving parts of the shell (snow-plough phase). In the right part of Eq. (A2) the first term is the acceleration of the shell element caused by pressure difference between the gas inside the remnant and the undisturbed external gas. The step function H is used here to set the external pressure to zero for shell elements which would otherwise contract supersonically. The second term in (A2) allows for momentum of the swept-up gas, and the third term is the element acceleration in the external gravitational field.

Neglecting the radiative cooling effects in the hot internal gas, the change of the thermal energy of the whole bubble can be written as follows:

$$\frac{{\rm d}E_{\rm th}}{{\rm d}t} = L_{\rm OB}(t) - \int\limits_S {\rm P}_{\rm in}\mathbf{U}\mathbf{n}\ {\rm d}S, \tag{A4}$$

where the integration is carried out over the shell surface. The mechanical luminosity of the parental OB-association $L_{\rm OB}(t)$ is believed to be constant during the assumed lifetime of the B stars (McCray & Kafatos 1987):

$$L_{\rm OB}(t) = \begin{cases} L_{\rm OB}, & t \le 30\,{\rm Myr}, \\ 0, & t > 30\,{\rm Myr}. \end{cases} \tag{A5}$$

The surface integral in Eq. (A4) represents work done by the hot internal gas for the shell expansion. In Eq. (A4) it is assumed that the thermal energy of the swept-up gas is radiated immediately after crossing the shock front and hence does not contribute to the thermal energy of the hot gas inside the remnant.

Eqs. (A1) – (A3) for each Lagrangian surface element along with Eq. (A4) for the whole bubble form a closed system of $7N+1$ ordinary first-order differential equations, which was solved numerically using the Adams prediction-correction method. We use the analytic solution of Weaver et al. (1977) for a spherical wind-driven bubble to specify the initial conditions:

$$U_0 = 0.6 \left(\frac{125 L_{\rm OB}}{154\pi\rho_{\rm c}}\right)^{\frac{1}{5}} t_0^{-\frac{2}{5}}, \tag{A6}$$

$$E_{\rm th,0} = \frac{5}{11} L_{\rm OB} t_0, \tag{A7}$$

$$t_0 = \left(\frac{154\pi\rho_{\rm c} R_0^5}{125 L_{\rm OB}}\right)^{\frac{1}{3}}, \tag{A8}$$

$$\kappa_0 = \frac{1}{3}\rho_{\rm c} R_0, \tag{A9}$$

where R_0, U_0 and κ_0 are the shell radius, velocity and surface mass density at the moment t_0. The initial thermal energy of the hot gas inside the remnant is denoted as $E_{\rm th,0}$. The quiescent gas density at the shell center is given by $\rho_{\rm c}$.

Appendix B: galactic model

Observations of the edge-on galaxies show that in disk galaxies the distribution of mass is well represented by a double exponential disk model (see e.g. de Grijs & van der Kruit 1996). Following this model, we assume that the galactic disk mass density, $\rho_{\rm d}$, is distributed as follows:

$$\rho_{\rm d}(r,z) = \frac{M_{\rm g}}{4\pi z_0 r_0^2} \exp\left(-\frac{r}{r_0}\right) \exp\left(-\frac{\mid z \mid}{z_0}\right), \tag{B1}$$

where $M_{\rm g}$ is the mass of the galactic disk, while r_0 and z_0 are length and height scales of the disk.

Kuijken & Gilmore (1989) solved the Poisson equation for such a density distribution and derived an associated gravitational potential:

$$\Phi(r,z) = -\frac{GM_{\rm g}}{z_0 r_0^3} \times \\ \times \int\limits_0^\infty \frac{J_0(kr)}{\left(r_0^{-2}+k^2\right)^{3/2}} \frac{z_0^{-1}{\rm e}^{-k|z|} - k{\rm e}^{-|z|/z_0}}{z_0^{-2}-k^2}\,{\rm d}k, \tag{B2}$$

where J_0 is the Bessel function of order 0.

The Z-component of gravitational acceleration $g_z = -\partial\Phi/\partial z$ can be expressed as

$$g_z(r,z) = -{\rm sign}(z)\frac{GM_{\rm g}}{z_0^2 r_0^3} \times \\ \times \int\limits_0^\infty \frac{J_0(kr)}{\left(r_0^{-2}+k^2\right)^{3/2}} \frac{{\rm e}^{-k|z|} - {\rm e}^{-|z|/z_0}}{z_0^{-2}-k^2} k\,{\rm d}k. \tag{B3}$$

We assume that the undisturbed galactic gas obeys a polytropic law and exists in hydrostatic equilibrium within the external gravitational field. Neglecting self-gravity of the gas and the radial component of the galactic gravitational field one can write the following equations:

$${\rm P}_{\rm th} = nkT, \tag{B4}$$

$${\rm P}_{\rm th} = {\rm P}_{\rm th,0}\left(\frac{\rho}{\rho_0}\right)^\gamma, \tag{B5}$$

$$\frac{{\rm dP}}{{\rm d}z} = -\rho\frac{{\rm d}\Phi}{{\rm d}z}. \tag{B6}$$

Here Φ is the gravitational potential. The polytropic index is given by γ. The mid-plane thermal pressure and density of the gas are denoted as ${\rm P}_{\rm th,0}$ and ρ_0. To close this system of equations we assumed that the total pressure, P, (with contributions from thermal, turbulent, magnetic field and cosmic ray components) is proportional to the thermal pressure, ${\rm P}_{\rm th}$:

$${\rm P} = C_{\rm pr}{\rm P}_{\rm th}, \tag{B7}$$

where $C_{\rm pr}$ is the proportionality coefficient. Finally, the connection between density, ρ, and number density, n, is given by $\rho = \mu n$.

The solution of Eqs. (B4) – (B7) for number density, temperature, and total pressure of the undisturbed medium can be written as:

$$n(z) = n_0 B^{-\frac{1}{1-\gamma}}(z), \tag{B8}$$

$$T(z) = T_0 B(z), \tag{B9}$$

$$P(z) = P_0 B^{-\frac{\gamma}{1-\gamma}}(z), \tag{B10}$$

where $B(z)$ denotes:

$$B(z) = 1 + \frac{\mu}{C_{\rm pr} k T_0} \frac{1-\gamma}{\gamma} \left[\Phi(z) - \Phi_0\right]. \tag{B11}$$

Here n_0, T_0, P_0, and Φ_0 are the number density, temperature, total pressure, and gravitational potential in the plane of galaxy.

Assuming a hot halo with temperature, $T_{\rm halo}$, at height, $z_{\rm halo}$, one can estimate the polytropic index, γ, from Eqs. (B9) and (B11) as

$$\gamma = \left(1 + \frac{C_{\rm pr} k}{\mu} \frac{T_{\rm halo} - T_0}{\Phi(z_{\rm halo}) - \Phi_0}\right)^{-1}. \tag{B12}$$

Appendix C: smoothed-plate shell projection

To project the simulated supershell onto the plane of view we represent every shell Lagrangian element as a mass particle spatially smoothed in three dimensions with characteristic lengths $\sigma_{x,i}, \sigma_{y,i}, \sigma_{z,i}$ corresponding to the shell element half-width, half-height, and half-thickness. The contribution of the i-th Lagrangian element to the total number density at the point with coordinates (x, y, z) becomes:

$$\Delta n_{{\rm s},i} = \frac{m_i}{(2\pi)^{3/2} \mu\, \sigma_{x,i}\sigma_{y,i}\sigma_{z,i}} \times \\ \times \exp\left\{-\frac{1}{2}\left[\left(\frac{x_i}{\sigma_{x,i}}\right)^2 + \left(\frac{y_i}{\sigma_{y,i}}\right)^2 + \left(\frac{z_i}{\sigma_{z,i}}\right)^2\right]\right\}. \tag{C1}$$

Here the (x_i, y_i, z_i) are coordinates of the given point in the local frame of reference (with the origin in the shell element center and X_i, Y_i, Z_i axes directed along the sides of the element); m_i is the mass of the shell element. The thickness of the shell was assumed to be one tenth of the element distance to the shell center.

The total number density at the given point is the sum of contributions from all elements:

$$n_{\rm s} = \sum_{i=1}^{N} \Delta n_{{\rm s},i}, \tag{C2}$$

where N is the number of shell elements. For computational efficiency, contributions to the sum (C2) are calculated only for elements which simultaneously meet the conditions:

$$|x_i| < 4\sigma_{x,i}; \quad |y_i| < 4\sigma_{y,i}; \quad |z_i| < 4\sigma_{z,i}. \tag{C3}$$

For any given point, the gas is assigned the mass-averaged value of radial velocity, $V_{\rm rad}$, from all contributing shell elements:

$$V_{\rm rad} = \frac{\sum \Delta n_{{\rm s},i} V_{{\rm rad},i}}{n_{\rm s}}. \tag{C4}$$

The column density of optically thin gas along a line of sight in the j-th velocity channel with central velocity, V_j, and channel half-width, $\sigma_{\rm f}$, can be written as follows:

$$N_j = \frac{1}{\sqrt{2\pi}} \left\{ \frac{1}{\sigma'_{\rm q}} \exp\left[-\frac{1}{2}\left(\frac{V_j - \frac{{\rm d}V_{\rm rad}}{{\rm d}x'} x'}{\sigma'_{\rm q}}\right)^2\right] \int n\, {\rm d}z' + \right. \\ \left. + \frac{1}{\sigma'_{\rm s}} \int \exp\left[-\frac{1}{2}\left(\frac{V_j - V_{\rm rad} - \frac{{\rm d}V_{\rm rad}}{{\rm d}x'} x'}{\sigma'_{\rm s}}\right)^2\right] n_{\rm s}\, {\rm d}z' \right\}. \tag{C5}$$

Here $\sigma'_{\rm q}$ and $\sigma'_{\rm s}$ denote $\sigma'_{\rm q} = \sqrt{\sigma_{\rm q}^2 + \sigma_{\rm f}^2}$ and $\sigma'_{\rm s} = \sqrt{\sigma_{\rm s}^2 + \sigma_{\rm f}^2}$, where $\sigma_{\rm q}$ and $\sigma_{\rm s}$ are the one-dimensional velocity dispersion of quiescent and shell gas, respectively. The average value of the radial velocity gradient along galactic line of nodes, ${\rm d}V_{\rm rad}/{\rm d}x'$, was introduced as a first approximation to take into account rotation of the galactic gas. The first integral in (C5) is calculated for the undisturbed gas outside the shell, while the second integral allows for the shell contribution. (x', y', z') is the observational frame of reference with the origin in the center of the shell. The x' axis is directed parallel to the galactic line of nodes, and the z' axis is directed towards the observer.

References

Betke M., Makris N.C., 1995, Fast Object Recognition in Noisy Images Using Simulated Annealing. In: Proceedings of the Fifth international conference on computer vision. Cambridge, MA, June 1995. IEEE Computer Society Press. P. 523.

Bisnovatyi-Kogan G.S., Blinnikov S.I., 1982, SvA 26, 530

Bisnovatyi-Kogan G.S., Silich S.A., 1991, SvA 35, 370

Bisnovatyi-Kogan G.S., Silich S.A., 1995, Reviews of Modern Physics 67, 661

Bomans D.J., Points S., Weis K., Chu Y.-H., 1995, Rev. Mex. Astron. Astrofis. Serie de Conferencias 3, 77

Bottema R., 1997, A&A 328, 517

Braun R., 1995, A&AS 114, 409

Brinks E., Bajaja E., 1986, A&A 169, 14

Chen Q., Defrise M., Deconick F., 1994, Symmetric Phase-Only Matched Filtering of Fourier-Mellin Transforms for Image Registration and Recognition. In: IEEE Transactions on Pattern Analysis and Machine Intelligence 16, 1156

Cornwell T., Braun R., 1989, Deconvolution. In: Synthesis Imaging in Radio Astronomy, Perley R.A., Schwab F.R., Bridle A.H. (eds.), published by the Astronomical Society of the Pacific, vol. 6, 167

de Grijs R., Peletier R., van der Kruit P., 1997, A&A 327, 966

de Grijs R., van der Kruit P.C., 1996, A&AS 117, 19

Deul E., den Hartog R., 1990, A&A 229, 362

Goudis C., Meaburn J., 1978, A&A 68, 189

Heckman T.M., Dahlem M., Lehnert M.D., Fabbiano G., Gilmore D., Waller W.H., 1995, ApJ 448, 98

Heiles C., 1979, ApJ 229, 533

Högbom J.A., 1974, A&AS 15, 417

Igumentshchev I.V., Shustov B.M., Tutukov A.V., 1990, A&A 234, 396

Kamphuis J., 1993, PhD thesis, Rijksuniversiteit, Groningen

Kamphuis J., Sancisi R., van der Hulst T., 1991, A&A 244, L29

Kuijken K., Gilmore, G., 1989, MNRAS 239, 571

Lee S.-W., Irwin J.A., 1997, ApJ 490, 247

Loeb A., Perna R., 1998, ApJ 503, L35

Mac Low M.-M., McCray R., 1988, ApJ 324, 776

Mac Low M.-M., McCray R., Norman M.L., 1989, ApJ 337, 141

Maciejewski W., Rozyczka M., 1993, Acta Astron. 43, 1

Mashchenko S.Y., Silich S.A., 1994, Astronomy Reports, 38, 207
McCray R., Kafatos M., 1987, ApJ 317, 190
Meaburn J., 1980, MNRAS 192, 365
Norman C., Ferrara A., 1997, ApJ 467, 280
Oey M.S., Clarke C.J., 1997, MNRAS 289, 570
Oey M.S., Massey P., 1995, ApJ 452, 210
Puche D., Westpfahl D., Brinks E., Roy J.-R., 1992, AJ 103, 1841
Ritter G., Wilson J., 1996, Handbook of Computer Vision Algorithms in Image Algebra, CRC Press, Boca Raton
Ryder S.D., Staveley-Smith L., Malin D., Walsh W., 1995, AJ 109, 1592
Silich S.A., 1992, Ap&SS 195, 317
Silich S.A., Mashchenko S.Y., Tenorio-Tagle G., Franco J., 1996, MNRAS 280, 711
Thilker D.A., 1998, Supershells in Spiral Galaxies. In: Franco J., Carraminana A. (eds.) Interstellar Turbulence, Proc. 2nd Guillermo Haro Conference (in press)
Thilker D.A., Braun R., Walterbos R.A.M., 1998a, A&A 332, 429 (TBW98)
Thilker D.A., Braun R., Walterbos R.A.M., Mashchenko S.Y., 1998b, in preparation.
Tomisaka K., 1992, PASJ 44, 177
Wang Q.D., Walterbos R.A.M., Steakley M.F., Norman C.A., Braun R., 1995, ApJ 439, 176
Weaver R., McCray R., Castor J., Shapiro P., Moore R. 1977, ApJ 218, 377